Multiband optical variability of the TeV blazar PG 1553 + 113 in 2019

Vinit Dhiman,[1,2]★ Alok C. Gupta [ID],[1,3]★ Sofia O. Kurtanidze,[4,5] I. Eglitis,[6] A. Strigachev,[7]
G. Damljanovic,[8] Paul J. Wiita,[9] Minfeng Gu,[3] Haritma Gaur,[1] Oliver Vince,[8] R. Bachev,[7] D. P. Bisen,[2]
S. Ibryamov [ID],[10] R. Z. Ivanidze,[4] Miljana D. Jovanovic [ID],[8] Omar M. Kurtanidze,[4,5,11]
M. G. Nikolashvili,[4,5] E. Semkov [ID],[7] B. Spassov,[7] M. Stojanovic,[8] Beatriz Villarroel,[12,13]
Haiguang Xu[14,15] and Zhongli Zhang[16,17,14]

[1]*Aryabhatta Research Institute of Observational Sciences (ARIES), Manora Peak, Nainital 263001, India*
[2]*School of Studies in Physics & Astrophysics, Pt. Ravishankar Shukla University, Amanaka G.E. Road, Raipur 492010, India*
[3]*Key Laboratory for Research in Galaxies and Cosmology, Shanghai Astronomical Observatory, Chinese Academy of Sciences, Shanghai 200030, China*
[4]*Abastumani Observatory, Mt. Kanobili, 0301 Abastumani, Georgia*
[5]*Landessternwarte, Zentrum für Astronomie der Universität Heidelberg, Königstuhl 12, D-69117 Heidelberg, Germany*
[6]*Institute of Astronomy, University of Latvia, Jelgavas 3, Riga, LV-1004, Latvia*
[7]*Institute of Astronomy and National Astronomical Observatory, Bulgarian Academy of Sciences, 72 Tsarigradsko Shosse Blvd., 1784 Sofia, Bulgaria*
[8]*Astronomical Observatory, Volgina 7, 11060 Belgrade, Serbia*
[9]*Department of Physics, The College of New Jersey, 2000 Pennington Rd., Ewing, NJ 08628-0718, USA*
[10]*Department of Physics and Astronomy, University of Shumen, 115, Universitetska Str., 9700 Shumen, Bulgaria*
[11]*Engelhardt Astronomical Observatory, Kazan Federal University, Tatarstan, Russia*
[12]*Nordita, KTH Royal Institute of Technology and Stockholm University, Roslagstullsbacken 23, SE-106 91 Stockholm, Sweden*
[13]*Instituto de Astrofisica de Canarias, Avda Via Lactea S/N, La Laguna, E-38205, Tenerife, Spain*
[14]*Shanghai Frontiers Science Center of Gravitational Wave Detection, 800 Dongchuan Road, Minhang, Shanghai 200240, China*
[15]*School of Physics and Astronomy, Shanghai Jiao Tong University, 800 Dongchuan Road, Minhang, Shanghai 200240, China*
[16]*Shanghai Astronomical Observatory, Chinese Academy of Sciences, Shanghai, 200030, China*
[17]*Key Laboratory of Radio Astronomy, Chinese Academy of Sciences, 210033 Nanjing, Jiangsu, China*

ABSTRACT

We report the flux and spectral variability of PG 1553 + 113 on intra-night (IDV) to short-term time-scales using BVRI data collected over 91 nights from 28 February to 8 November 2019 employing 10 optical telescopes: three in Bulgaria, two each in India and Serbia, and one each in Greece, Georgia, and Latvia. We monitored the blazar quasi-simultaneously for 16 nights in the V and R bands and 8 nights in the V, R, I bands and examined the light curves (LCs) for intra-day flux and colour variations using two powerful tests: the power-enhanced F-test and the nested ANOVA test. The source was found to be significantly (>99 per cent) variable in 4 nights out of 27 in R-band, 1 out of 16 in V-band, and 1 out of 6 nights in I-band. No temporal variations in the colours were observed on IDV time-scale. During the course of these observations the total variation in R-band was 0.89 mag observed. We also investigated the spectral energy distribution (SED) using B-, V-, R-, and I-band data. We found optical spectral indices in the range of 0.878 ± 0.029 to 1.106 ± 0.065 by fitting a power law ($F_\nu \propto \nu^{-\alpha}$) to these SEDs of PG 1553 + 113. We found that the source follows a bluer-when-brighter trend on IDV time-scales. We discuss possible physical causes of the observed spectral variability.

Key words: galaxies: active – BL Lacertae objects: general – BL Lacertae objects: individual: PG 1553 + 113 – quasars: individual.

1 INTRODUCTION

The blazar sub-class of radio-loud (RL) active galactic nuclei (AGN) possess a relativistic jet aligned at an angle of $\leq 10°$ from the observer's line of sight (Urry & Padovani 1995). The Doppler enhanced intense non-thermal radiation from this jet dominates the spectral energy distribution (SED) from radio to very high energy (VHE) γ-ray energies. Blazars are usually considered to be comprised of both of BL Lacertae (BL Lac) objects, and flat

spectrum radio quasars (FSRQs). Blazars show flux and spectral variability across the entire electromagnetic (EM) spectrum, emit predominantly non-thermal radiation showing strong polarization from radio to optical (>3 per cent) frequencies, and usually have core dominated radio structures.

The multiwavelength (MW) SEDs of blazars in the usual $\log(\nu F_\nu)$ vs $\log(\nu)$ representation show double-humped structures in which the low energy hump peaks in infrared (IR) through X-ray bands while the high energy hump peaks in γ-rays energies (Fossati et al. 1998). The location of SED peaks are often used to classify blazars into two sub-classes namely LBLs (low-energy-peaked blazars) and HBLs (high-energy-peaked blazars). In LBLs, the first hump peaks in IR

to optical bands and the second hump peaks at GeV γ-ray energies. In HBLs, the first hump peaks in UV to X-ray bands and the second hump is located up to TeV γ-ray energies (Padovani & Giommi 1995). The emission of the lower energy SED is due to synchrotron radiation which originates from relativistic electrons in the jet but the high energy portion of the SED can arise in several ways.

Flux variability over a wide range of time-scales is one of the definitional properties of blazars. On the basis of the times over which it is observed, blazar variability can be divided into three classes: microvariability (Miller, Carini & Goodrich 1989) or intra-day variability (IDV; Wagner & Witzel 1995) or intra-night variability (Gopal-Krishna, Sagar & Wiita 1993; occurring on a time-scale of a few minutes to less than a day); short-term variability (STV; taking place on a time-scale of days to months); and long-term variability (LTV; over a time-scale of several months to years or even decades (Gupta et al. 2004). The first clear optical IDV detection was reported in the light curves of the blazar BL Lacertae (Miller et al. 1989). Since then the optical variability of blazars on diverse time-scales have been studied extensively and reported in many series of papers (e.g. Miller et al. 1989; Carini, Miller & Goodrich 1990; Carini et al. 1992; Xie et al. 1992, 1994, 2002; Heidt & Wagner 1996; Sillanpaa et al. 1996a, b; Fan et al. 1997, 1998; Raiteri et al. 1998; Bai et al. 1998; Fan, Qian & Tao 2001; Stalin et al. 2005; Gu et al. 2006; Gupta et al. 2008, 2016a, 2017, 2019; Bachev et al. 2012; Gaur et al. 2012b, c, 2015, 2019; Agarwal & Gupta 2015; Agarwal et al. 2016, 2019; Pandey et al. 2019, 2020a, b and references therein). In the optical regime, HBLs are found to be less variable than LBLs and their variability amplitudes are also much smaller than that of LBLs (Jannuzi, Smith & Elston 1994; Gaur, Gupta & Wiita 2012a; Gaur et al. 2012b). Measurements of variability amplitudes and duty cycles, temporal lags between bands, along with spectral changes, can provide information about the location, size, structure, and dynamics of the regions emitting non-thermal photons.

PG 1553 + 113 was discovered by the Palomar-Green survey of UV-excess stellar objects (Green, Schmidt & Liebert 1986) and was classified as a BL Lac object due to its featureless optical spectrum and significant optical variability (Miller & Green 1983). Furthermore, it was classified as an HBL, as its synchrotron emission peak falls in the UV and X-ray frequency ranges (Falomo & Treves 1990) and it was detected at TeV energies (Aharonian et al. 2006). The recent detection of its putative galaxy group would set this object's redshift at $z = 0.433$ (Johnson et al. 2019). Being relatively bright and with intriguing flux variability, over the past two decades PG 1553 + 113 has been extensively studied in single EM bands in isolation (e.g. Pandey et al. 2019; Pasierb et al. 2020; Agarwal et al. 2021) or in simultaneous/quasi-simultaneous MW observations on diverse time-scales (e.g. Ackermann et al. 2015; Dhiman et al. 2021). An optical flare was observed in April 2019 when it showed the brightest magnitude of 13.2 in the R-band over the period 2005–2019 (Agarwal et al. 2021). On IDV time scales, it has shown significant variation in linear polarization percentage and position angle (Andruchow et al. 2011).

PG 1553 + 113 is among a few blazars which have been claimed to show occasional periodic/quasi periodic oscillations in the light curves in different EM bands on diverse time-scales. The first claim of 2.18 ± 0.08 years periodicity was reported in the γ-ray, optical, and radio light curve (LCs) of the source (Ackermann et al. 2015). This period in γ-rays was confirmed by (Prokhorov & Moraghan 2017; Tavani et al. 2018; Sandrinelli et al. 2018; Covino et al. 2020; Peñil et al. 2020) and also confirmed in the optical R-band (Sandrinelli et al. 2018; Covino et al. 2020). Recently Agarwal et al. (2021) reported a median period of 2.21 ± 0.04 yr using the historical optical light curves which confirms the results of (Ackermann et al. 2015); an

additional secondary period of about 210 days was also detected and a spectral index $\alpha = 0.89 \pm 0.06$ was found (Agarwal et al. 2021).

This paper is organized as follows: Section 2 provides an overview of the telescopes, photometric observations, and the data reduction procedure. Analysis techniques we used to search for flux variability and correlations between bands are discussed in Section 3. Results of our study are reported in Section 4. A discussion and conclusions are provided in Section 5.

2 OBSERVATIONS AND DATA REDUCTION

In 2019, the TeV blazar PG 1553 + 113 was observed using 10 optical ground-based telescopes located in 6 countries (India, Georgia, Greece, Bulgaria, Serbia, and Latvia). Key details about these telescopes are given in Table 1. These telescopes are equipped with CCD detectors and UBVRI broadband optical filters (Gaur et al. 2012b, 2015; Gupta et al. 2016a). Extensive photometric observations of PG 1553 + 113 were carried out using these 10 telescopes from late February to early November 2019. The detailed observation log is given in Table A1.

The data obtained from the Indian, Latvian, and Greek telescopes were processed using the same data reduction steps. For the processing of the raw data, we used standard procedures of the Image Reduction and Analysis Facility (IRAF)[1] software following the steps described below. For image pre-processing, we generated a master bias frame for each observing night which was subtracted from all twilight flat frames and all source image frames taken on that particular night. A master flat was generated for each filter by taking the median of all the bias subtracted twilight sky flat frames and then normalizing the master flat. To remove pixel-to-pixel inhomogeneity, the source image was divided by the normalized master flat of the same filter. Finally, cosmic ray removal was carried out for all source image frames. To find the instrumental magnitudes of the blazar PG 1553 + 113 and its local standard stars (see fig. 1, Raiteri et al. 2015) we employed a concentric circular multi-aperture photometry technique using the DAOPHOT software II[2] (Stetson 1987, 1992). Explicitly, for the aperture photometry, we took four different concentric aperture radii i.e. $1 \times$ FWHM (full width at half-maximum), $2 \times$ FWHM, $3 \times$ FWHM, and $4 \times$ FWHM for every night. In several earlier studies, we have found that the aperture radii $= 2 \times$ FWHM provides the best S/N (e.g. Gupta et al. 2016a; Pandey et al. 2019, references therein), so we used this value for our final analysis. Image processing of data obtained from the Bulgarian and Georgian telescopes was performed using ESO-MIDAS2[3] (Gaur et al. 2012b) and MAXIMDL[4] is used for the Serbian telescopes (Pandey et al. 2020a), respectively, in a similar fashion that IRAF was used on the observations from the Indian, Latvian, and Greek telescopes.

In every night of observations we observed all four local standard stars on the same field (see fig. 1 of Raiteri et al. 2015). We selected two standard stars, Stars 2 and 3 from fig. 1 of (Raiteri et al. 2015)). These two standard stars have magnitudes and colours close to that of the target blazar. Finding such ideal standard stars in blazar fields are rare. Using these stars for calibrating the blazar magnitude will

---

[1]IRAF is distributed by the National Optical Astronomy Observatories, which are operated by the Association of Universities for Research in Astronomy, Inc., under cooperative agreement with the National Science Foundation.
[2]Dominion Astrophysical Observatory Photometry software.
[3]ESO-MIDAS is the European Southern Observatory Munich Image Data Analysis System which is maintain and developed by European Southern Observatory.
[4]https://diffractionlimited.com/help/maximdl/MaxIm-DL.htm

Table 1. Details of telescopes and instruments used.

	A1	A2	AS1	AS2	G
Telescope	1.30-m DFOT	1.04-m ST	60-cm ASV	1.4-m ASV	70 cm meniscus telescope
CCD model	Andor 2K CCD	STA4150	CCD FLI PL230	Andor iKon-L	FLI-4240
Chip size (pixels)	2048×2048	4096×4096	2048×2064	2048×2048	2048×2048
Scale (arcsec/pixel)	0.535	0.264	0.518	0.244	2.4
Field (arcmin^2)	18×18	16×16	17.7×17.8	8.3×8.3	15×15
Gain (e$^-$/ADU)	2.0	3.49	1.8	1	8
Read-out noise (e$^-$ rms)	7.0	6.98	18.6	7	10
Typical seeing (arcsec)	1.2–2.0	1.2–2.5	1–2	1–2	1.0–2.0
	R1	R2	B	BS	S
Telescope	50/70-cm NAO	2m RC NAO	60-cm AO	Baldone Schmidt	1.3m Modified RC
CCD model	FLI PL16803	VersArray:1300B	FLI PL9000	STX-16803	Andor CCD DZ936-BXDD
Chip size (pixels^2)	4096×4096	1340×1300	3056×3056	4096×4096	2048×2048
Scale (arcsec/pixel)	1.079	0.258	0.33	0.78	0.2829
Field (arcmin^2)	73.66×73.66	5.76×5.76	16.8×16.8	53×53	9.6×9.6
Gain (e$^-$/ADU)	1	1	1	1.33	0.8650
Read-out noise (e$^-$ rms)	9	2	9	10	5.95
Typical seeing (arcsec)	2–4	1.5–2.5	1.5–2.5	2–4	1–1.3

A1: 1.3-m Devasthal Fast Optical Telescope (DFOT) at ARIES, Nainital, India
A2: 1.04-m Samprnanand Telescope(ST), ARIES, Nainital, India
AS1: 60-cm Cassegrain Telescope, Astronomical Station Vidojevica (ASV), Serbia
AS2: 1.4-m telescope located at Astronomical Station Vidojevica, Serbia
G: 70-cm meniscus telescope at Abastumani Observatory, Georgia
R1: 50/70-cm Schmidt Telescope at National Astronomical Observatory Observatory, Rozhen, Bulgaria
R2: 2-m Ritchey-Chretien telescope at National Astronomical observatory Rozhen, Bulgaria
B: 60-cm Cassegrain Telescope at Astronomical Observatory Belogradchik, Bulgaria
BS: 1.20-m Baldone Schmidt Telescope at the Institute of Astronomy, University of Latvia
S: 1.3-m Skinakas Observatory, Crete, Greece

avoid any error occurring from differences in the photon statistics in the differential photometry of the blazar and standard stars. Since the magnitudes of PG 1553 + 113 and the standard stars were obtained simultaneously under the same air mass and weather conditions, there is no need for correction of atmospheric extinction. Finally one comparison star (Star 2) was used to calibrate the instrumental magnitude of PG 1553 + 113.

3 ANALYSIS TECHNIQUES

To examine the frequency of intra-day variability of the blazar PG 1553 + 113 from these optical data, we have employed two different analysis techniques: power enhanced F-test and nested analysis of variance (ANOVA). These are more reliable methods for quantifying variabilty than the earlier widely used statistical tests such as the standard F-test and C-test (de Diego 2014; de Diego et al. 2015). Both of these methods use several comparison stars in the analysis. We also examine the amplitudes and duty cycles of its optical variability and perform cross-correlation analyses between bands.

3.1 Power-enhanced F-test

To obtain the optical intra-day variability in the blazar PG 1553 + 113, our use of the power-enhanced F-test followed the approach given in de Diego (2014) and de Diego et al. (2015). This test has frequently been used in recent studies for finding IDV in blazars (e.g. Gaur et al. 2015; Polednikova et al. 2016; Kshama, Paliya & Stalin 2017; Pandey et al. 2019, 2020a, and references therein). In this test we compare the variance of the source LC to the combined variance of those of all standard stars. We used the closest brightest star to the object as our reference star to minimize errors. The other standard stars in the blazar field are considered as the comparison stars. The enhanced F-test is defined as $F_{enh} = s_{blz}^2/s_c^2$

(de Diego 2014) where $s_c^2 = \frac{1}{(\sum_{j=1}^{k} N_j)-k} \sum_{j=1}^{k} \sum_{i=1}^{N_i} s_{j,i}^2$. Here, s_{blz}^2 is the variance of differential light curve (DLC) of the blazar and reference star, and s_c^2 is the stacked variance of the comparison star-reference star DLCs (de Diego 2014), where N_j is the number of observations of the jth star and k is the total number of comparison stars; $s_{j,i}^2$ is the scaled square deviation, which for the jth comparison star is defined as $s_{j,i}^2 = \omega_j(m_{j,i} - \bar{m}_j)^2$, where ω_j, $\bar{m}_j$, and $m_{j,i}$, are the scaling factor, the mean magnitude of the jth comparison star DLC, and differential magnitude, respectively. The scaling factor ω_j is taken as the ratio of averaged square error of the blazar-reference star DLC to the averaged square error of the differential instrumental magnitudes in the comparison star-reference star DLC (Joshi et al. 2011). As ω_j is the ratio of the errors, it cancels out the too small (by factors of ~1.5) photometric errors that emerge from IRAF (Stalin et al. 2004; Goyal et al. 2013). The degree of freedom in the denominator is increased by the stacking of the variances of the comparison stars so the power of the power-enhanced F-test is enhanced when compared to the often previously used simple F-test.

In this work, we have three comparison field stars (S2, S3, and S4) from which star S2, having magnitude closest to the source's instrumental magnitude, is considered to be the reference star, and the remaining ($k = 2$) field stars as the comparison stars. Since the blazar and all the comparison stars have the same number of observations (N), the number of degrees of freedom in the denominator and numerator in the power-enhanced F-statistics are $\nu_1 = N - 1$ and $\nu_2 = k(N - 1)$, respectively. Then the F_{enh} value is computed and compared with the critical value (F_c) at $\alpha = 0.01$, where α is the significance level set for the test, corresponding to a confidence level of 99 per cent. Such a low α value, indicates that the probability that the result arises by chance is very small. If F_{enh} is larger than the critical value, the null hypothesis (no variability) is discarded. The estimated values of F_{enh} and F_c are given in Tables 2 and B1.
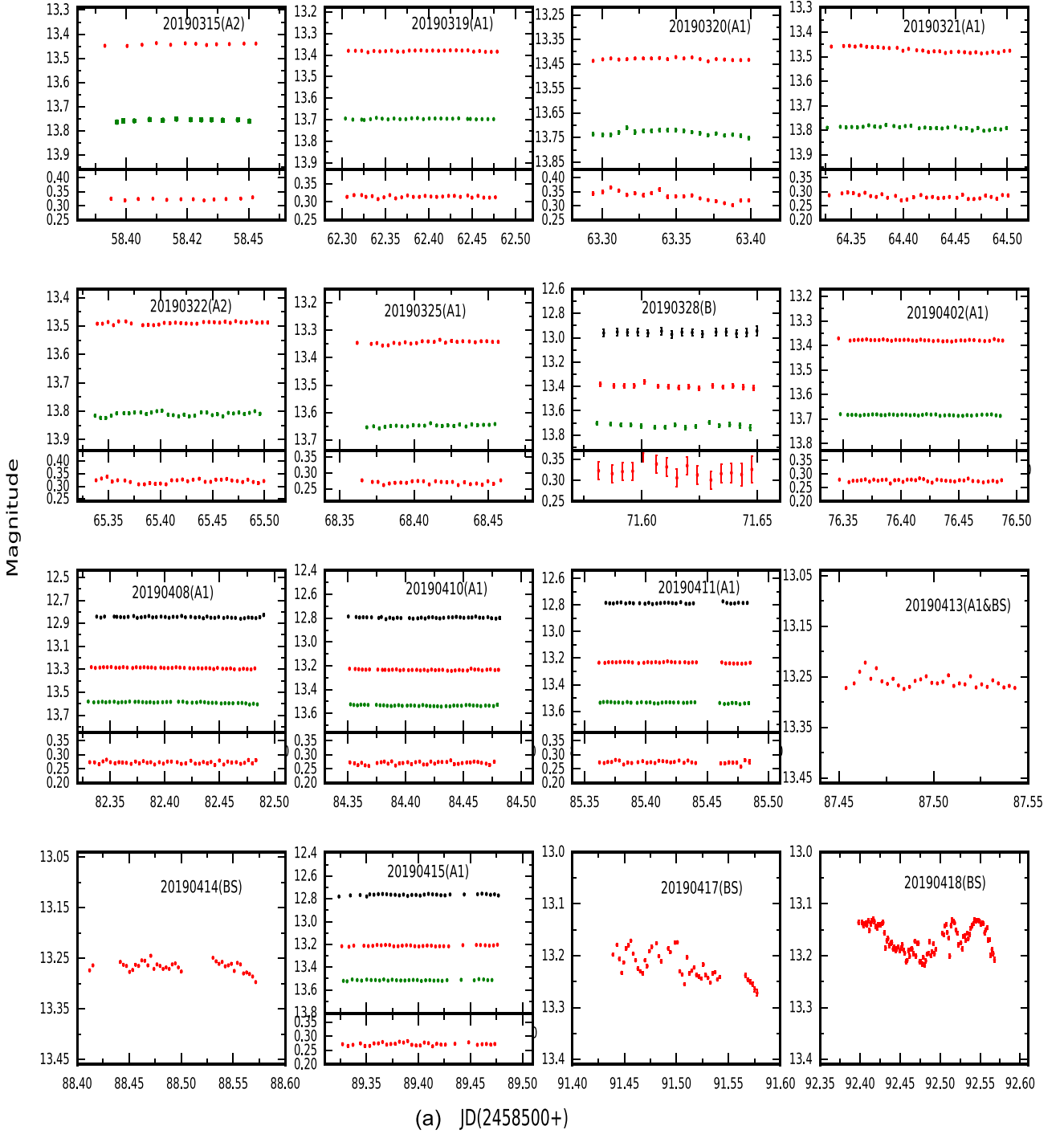
Figure 1. Upper sub-panels display IDV optical (VRI) light curves of PG 1553 + 113; they are shown in green (V), red (R), and black (I), respectively; bottom sub-panels show the colour (V−R) variation on IDV time-scales. The date of observations and the telescope abbreviation are given in each panel.

3.2 Nested ANOVA test

The one-way ANOVA test for AGN variability was introduced by de Diego et al. (1998). The nested ANOVA test is an updated version of the ANOVA test which uses several stars as reference stars to generate different DLCs of the blazar. In contrast to power-enhanced F-test, no distinct comparison star is needed for the nested ANOVA test, and all the comparison stars are used as reference stars, so the number of stars in the analysis is increased by one (de Diego et al. 2015; Pandey et al. 2019). The nested ANOVA test compares

the average of dispersions between the groups of observations. In our case, we have used three reference stars (2, 3, and 4 which we call here as S2, S3, and S4, respectively)[5] to generate DLCs of the blazar. These three DLCs are then divided into a number of groups with four points in each group. A disadvantage of this technique is that microvariations shorter than the lapse time within each group
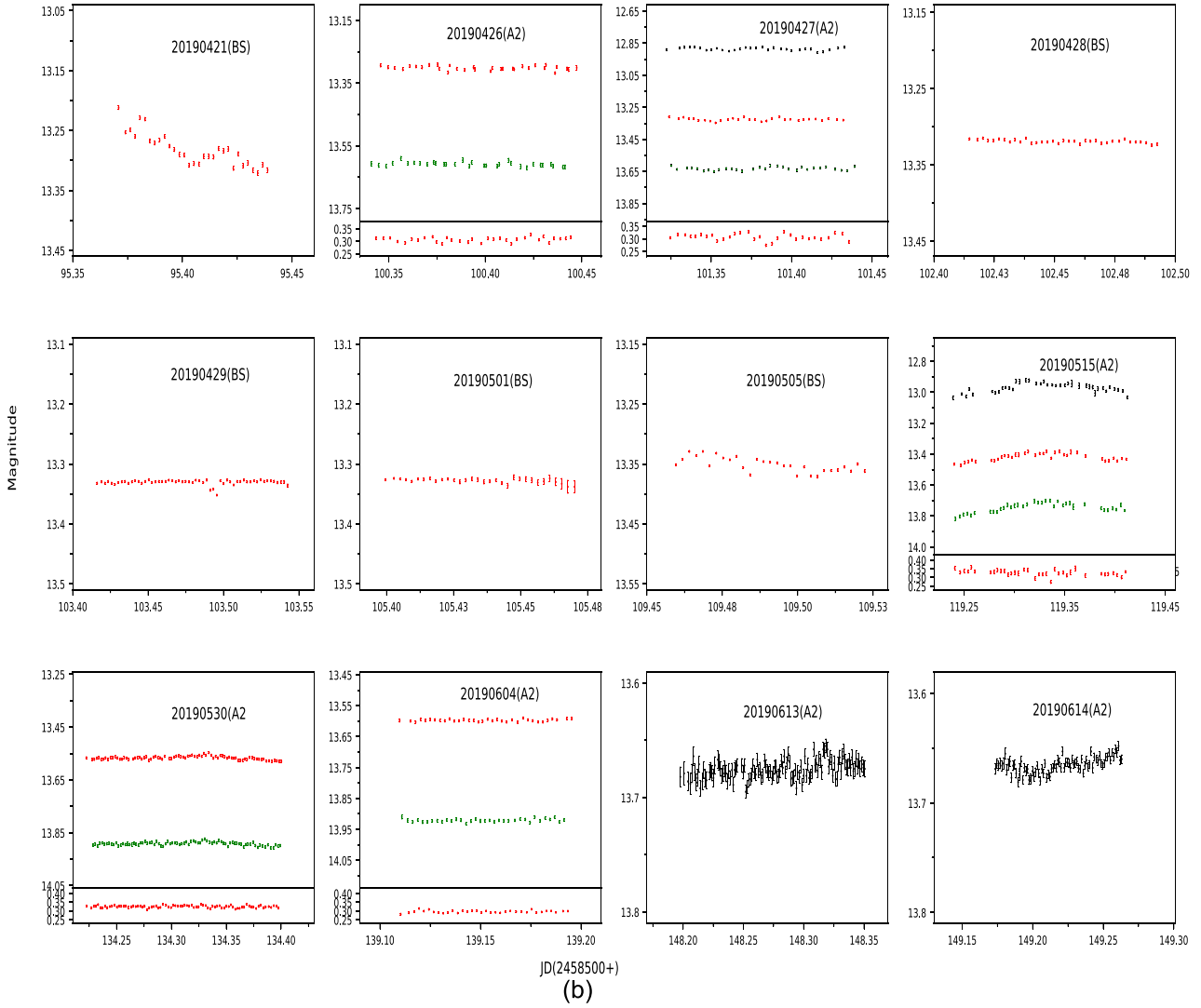
[5] https://www.lsw.uni-heidelberg.de/projects/extragalactic/charts/1553+113.html

(b)

Figure 1. *– continued*

Table 2. Results of IDV analysis of PG 1553 + 113.

Observation date yyyy-mm-dd	Band	*Power-enhanced F-test* DoF(v_1, v_2)	F_{enh}	F_c	*Nested ANOVA* DoF(v_1, v_2)	F	F_c	Status	Amplitude per cent
20190417	R	47, 94	2.78	1.76	11, 36	9.44	2.79	V	14.98
20190418	R	102, 204	2.93	1.48	19,80	4.19	2.14	V	8.89
20190515	V	35, 70	6.53	1.93	6, 28	10.36	3.52	V	11.82
	R	35, 70	3.13	1.93	6, 28	8.57	3.52	V	9.02
	I	35, 70	3.21	1.93	6, 28	3.75	3.52	V	8.19
20190613	R	123, 246	1.97	1.43	23, 96	2.65	2.00	V	3.91

of observations cannot be detected by the nested ANOVA test. But such phenomena, known as spikes, have been seldom reported in the literature (e.g. Sagar, Gopal-Krishna & Wiita 1996; de Diego et al. 1998; Stalin et al. 2004).

To get the results, we used our own PYTHON program for this test. Following equation (4) of de Diego et al. (2015) we calculated the mean square due to groups (MS_G) and mean square due to nested observations in groups ($MS_{O(G)}$). The ratio $F = MS_G/MS_{O(G)}$ follows an F distribution with $a - 1$ and $a(b - 1)$ degrees of freedom, in

the numerator and denominator, respectively, where a is the number of groups in an observation and b is the number of data points in each group. A light curve is considered as variable if the value of F-statistic $\geq F_c$ at 99 per cent confidence level, otherwise, we call it non-variable. The results of both the statistical tests are given in Tables 2 and B1, where an LC is conservatively labeled as variable (V) only if both the tests found significant variations in it, otherwise it is labeled as NV, though of course there may be weak intrinsic variability even in some of those cases.

3.3 Intraday variability amplitude

For each of the variable light curves, we calculated the flux variability amplitude (Amp), using the equation given by (Heidt & Wagner 1996).

$$Amp = 100 \times \sqrt{(A_{\max} - A_{\min})^2 - 2\sigma^2}, \quad (1)$$

where $A_{\max}$ and $A_{\min}$ are the maximum and minimum magnitudes, respectively, in the calibrated light curves of the blazar, while σ is the mean error. The amplitude of variability is also mentioned in the last column of Table 2 for the variable light curve.

3.4 Duty cycle

The duty cycle (DC) provides a direct estimation of the fraction of time for which a source has shown variability. We have estimated the DC of PG 1553 + 113 by using the standard approach (Romero, Cellone & Combi 1999). For these DC calculations, we considered only those LCs which were continuously monitored for at least about 1.5 h, with

$$DC = 100 \frac{\sum_{i=1}^{n} N_i(1/\Delta t_i)}{\sum_{i=1}^{n}(1/\Delta t_i)} \text{per cent} \quad (2)$$

here $\Delta t_i = \Delta t_{i, obs}(1 + z)^{-1}$ is the redshift corrected observing time of the source during the *ith* observation, and N_i takes the value 1 if IDV is detected or 0 if not detected. Computation of the DC has been weighted by the observing time Δt_i for the ith observation, as the observation time is different for each observation.

3.5 Discrete correlation function

There may be time lags between the observed light curves in different optical bands. To examine this possibility, we used the Discrete Correlation Function (DCF) given by Edelson & Krolik (1988) which is an useful analysis tool for unevenly sampled astronomical data. To get better estimations of errors, the technique was modified by (Hufnagel & Bregman 1992). Using the method, firstly we calculate the unbinned correlation (UDCF) using the given time series by

$$UDCF_{ij} = \frac{(x(i) - \bar{x})(y(j) - \bar{y})}{\sqrt{\sigma_x^2 \sigma_y^2}}, \quad (3)$$

where $\bar{x}$ and $\bar{y}$ are the mean values of the two discrete data series $x(i)$ and $y(j)$, with standard deviations σ_x^2 and σ_y^2 and measurement errors e_x, e_y. After calculation of the UDCF, the correlation function is binned. Averaging the UDCF values (N in number) for each time delay, τ, to calculate the DCF,

$$DCF(\tau) = \frac{1}{N} \sum UDCF_{ij}. \quad (4)$$

where τ is the center of the bin of size $\Delta\tau$. The error is found from the standard deviations of the number of bins used for determining the DCF and is given as

$$\sigma_{DCF}(\tau) = \frac{\sqrt{\sum[UDCF_{ij} - DCF(\tau)]^2}}{N - 1}. \quad (5)$$

A positive DCF peak implies that the data from the two different EM bands are correlated, while two data sets are anti-correlated if DCF value < 0, but no DCF peak or DCF = 0 implies that no correlation exists between the two different EM bands data. When correlating a data series with itself (i.e. $x = y$), we obtain an autocorrelation function (ACF) with an automatic peak at $\tau = 0$, indicating the absence of any time lag. For an ACF, any other strong peak can indicate the presence of periodicity (Pandey, Gupta & Wiita 2017).

4 RESULTS

Our optical photometric observations of the TeV blazar PG 1553 + 113 were carried out during a total of 91 distinct nights from 28 February to 8 November 2019 using 10 optical telescopes listed in Table 1. One or more of these telescopes observed the source quasi-simultaneously in B-, V-, R-, and I-bands in 43 nights, in V-, R-, and I-bands in 2 nights, in V- and R-bands in 1 night, and in only in the single R-band on 67 nights. In total, 2418 image frames were obtained during the complete observational period of which 77, 615, 1437, and 289 image frames were in the B-, V-, R-, and I-bands, respectively. Now we present the results of the variability properties of this blazar carried out on IDV and STV time-scales.

4.1 Intraday variability

4.1.1 Intraday flux variability

We plot the calibrated V-, R-, and I-band magnitude versus time IDV LCs for the blazar PG 1553 + 113 in the upper panels of Fig. 1; when available, the V−R colour versus time plots are in the lower panels. To search for the clear presence of IDV, we performed the statistical tests discussed in Sections 3.1 and 3.2. The complete results of this analysis are given in Table B1.

Significant IDV was detected in R-band LCs of PG 1553 + 113 on April 17, 18, and June 13. On May 15, we found IDV in all of the V-, R-, and I-bands. Notice that the errors in the V-band LCs are roughly twice as large as those in R, so this reduces the likelihood of detecting any small variations that might be present. We also estimated the IDV amplitudes for the confirmed variable LCs, shown in the last column of Table 2 using equation (1). Usually a blazar's variability amplitude is larger at higher frequencies, as seen in this case on 15 May 2019 in which I-, R-, and V-band all showed variability. This trend suggests that the blazar spectrum gets steeper with decreasing brightness and flatter with increasing brightness (e.g. Massaro et al. 1998; Agarwal & Gupta 2015). However, on some occasions the variability amplitude of blazars at lower frequencies was found to be comparable or even larger than that at higher frequencies (e.g. Ghosh et al. 2000; Gaur et al. 2015).

4.1.2 Intraday cross-correlated flux variability

We have used the DCF technique as described in Section 3.5 to determine the cross correlations and thus search for any time lags between the V, R, and I optical bands for 2019 May 15, the only night in which we observed IDV variation from all bands. We took a DCF bin size of 12 min and get strong peaks (with DCFs ∼ 1) at an essentially zero lag, as is clear from Fig. 2. The null time lags imply that the photons in these wavebands are emitted by the same physical processes and from the same emitting region, which is not surprising, given how close in frequency these optical bands are used the interpolated cross-correlation function and found no significant time lag between the different optical bands (e.g. Agarwal & Gupta 2015; Agarwal et al. 2016; Bachev et al. 2017, and references therein).

4.1.3 Intraday duty cycle

Agarwal et al. (2021) carried out an optical IDV literature survey which included 28 new optical IDV light curves of PG 1553 + 113. A total of 74 optical IDV observations carried out during 1999–2019 were discussed there and in them the source showed IDV in eight
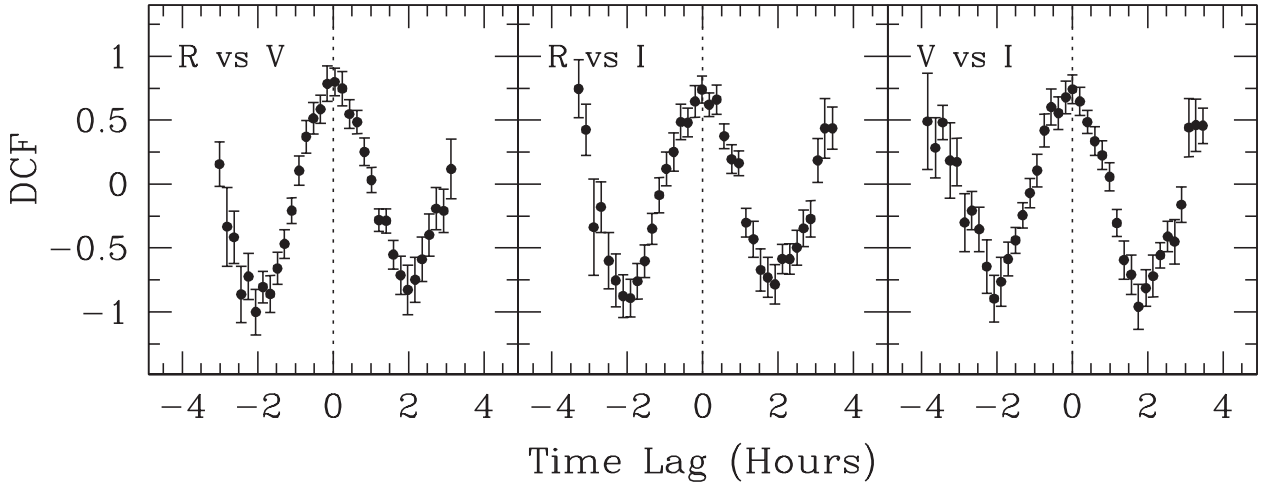
Figure 2. DCF plots for PG 1553 + 113 on 2019 May 15 showing peaks consistent with 0 lag. In each plot, *X*- and *Y*-axis are the time lags in hours and DCF values, respectively.

nights i.e. DC = 10.8 per cent. In our current work we have 50 IDV LCs taken in 27 observing nights. We found 4 variable IDV LCs out of 27 LCs in the R-band, 1 variable IDV LC out of 17 LCs in the V-band, and 1 variable IDV LC out of 6 LCs in the I-band. The DCs for the R-, V-, and I-bands are 14.8 per cent, 5.88 per cent, and 16.7 per cent, respectively. Combining them, the DC of PG 1553 + 113 based on all these new IDV LCs is 12 per cent, which is consistent with the previous results (e.g. Agarwal et al. 2021, and references therein).

4.1.4 Intraday colour variation

To study colour variation of the TeV blazar PG 1553 + 113 on IDV time-scales with respect to time and V-band magnitude (colour magnitude variation), we can use the 16 nights of data on which quasi-simultaneous observations were carried out in V and R-bands. We calculated the V−R colour indices (CIs) for each pair of V and R magnitudes and plotted these V−R CIs with respect to time in the bottom panel of Fig. 1, and our results are presented in the last column of Tables 2 and B1.

To investigate the colour behaviour of PG 1553 + 113 with respect to V-band magnitude [colour–magnitude (CM) plot], we fitted a straight line of the form CI = mV + C on each CM plot, which are displayed for each night in Fig. 3, with the results listed in Table 3. Clear global brighter-when-bluer (BWB) trends were observed in 11 nights on IDV time-scales, with correlation coefficients ranging between 0.5 and 0.9. Hence this source's brightness was found to have strong BWB chromatism on IDV time-scales. Such a BWB trend has been found to be predominant in BL Lac objects in the large number of optical observations made during both flaring and steady states (e.g. Ghosh et al. 2000; Gu et al. 2006; Gaur et al. 2012c). Villata et al. (2004a) found that the intra-day flares followed a BWB trend strongly, with a slope of ∼ 0.4, which is also the case for our data, with the slopes of the IDV LCs more than ∼ 0.5 in majority of cases.

A bluer-when-brighter (BWB) trend is commonly observed in blazars (e.g. Clements & Carini 2001; Raiteri et al. 2001; Villata et al. 2002; Papadakis et al. 2003; Papadakis, Villata & Raiteri 2007; Rani et al. 2010; Agarwal & Gupta 2015), in particular blazars of the HSP class, in which the optical continuum is generally believed to be entirely dominated by the non-thermal jet synchrotron emission, and can be explained in shock-in-jet models. In LSP blazars, in

which the accretion disc can provide a contribution to the optical continuum, a RWB trend sometimes is seen and probably indicates a relatively increasing thermal contribution at the blue end of the spectrum when the non-thermal jet emission decreases (e.g. Villata et al. 2006; Raiteri et al. 2007; Gaur et al. 2012c).

4.2 Short term variability

4.2.1 Short term flux variability

The STV light curves of PG 1553 + 113 in B-, V-, R-, and I-bands for the entire monitoring period are shown in Fig. 4, where we have plotted the nightly averaged magnitudes in B-, V-, R-, and I-bands with respect to time. During our monitoring period the source was detected in the brightest state of R = 13.13 mag on April 18, while the faintest level detected was R = 14.02 mag on September 29. The mean magnitudes were 14.23, 13.83, 13.51, and 13.07 in B-, V-, R-, and I-bands, respectively. The variability on STV time-scales can be clearly seen at all optical wavelengths. Using equation 1, we have estimated very similar variability amplitudes of 83.7 per cent, 75.9 per cent, 75.8 per cent, and 72.3 per cent, respectively, in B-, V-, R-, and I-bands.

4.2.2 Spectral variability

The CM relationship can be useful for exploring various variability scenarios and better understanding the origin of blazar emission. Therefore, we searched for any relationship of the source's colour indices (CIs) with brightness in the R-band and with respect to time. We fitted the plots of the optical CIs such as (B−V), (B−I), (V−R), and (R−I) with respect to both R-band magnitude and time along a straight line of the form Y = mX + C as shown in Figs 5 and 6, respectively (Pandey et al. 2020b). Values of the parameters associated with these colour-time and CM plots are given in Tables 4 and 5, respectively. We found B−V and B−I colours to show highly significant variation with time as well as R magnitude, while the CIs involving the R-band show weaker trends in the same directions. A positive slope defines a significant positive correlation between CIs and blazar R magnitude, meaning that the source follows a bluer-when-brighter (BWB) trend, while a negative slope defines redder-when-brighter (RWB) trend (e.g. Gupta et al. 2017, and references therein).
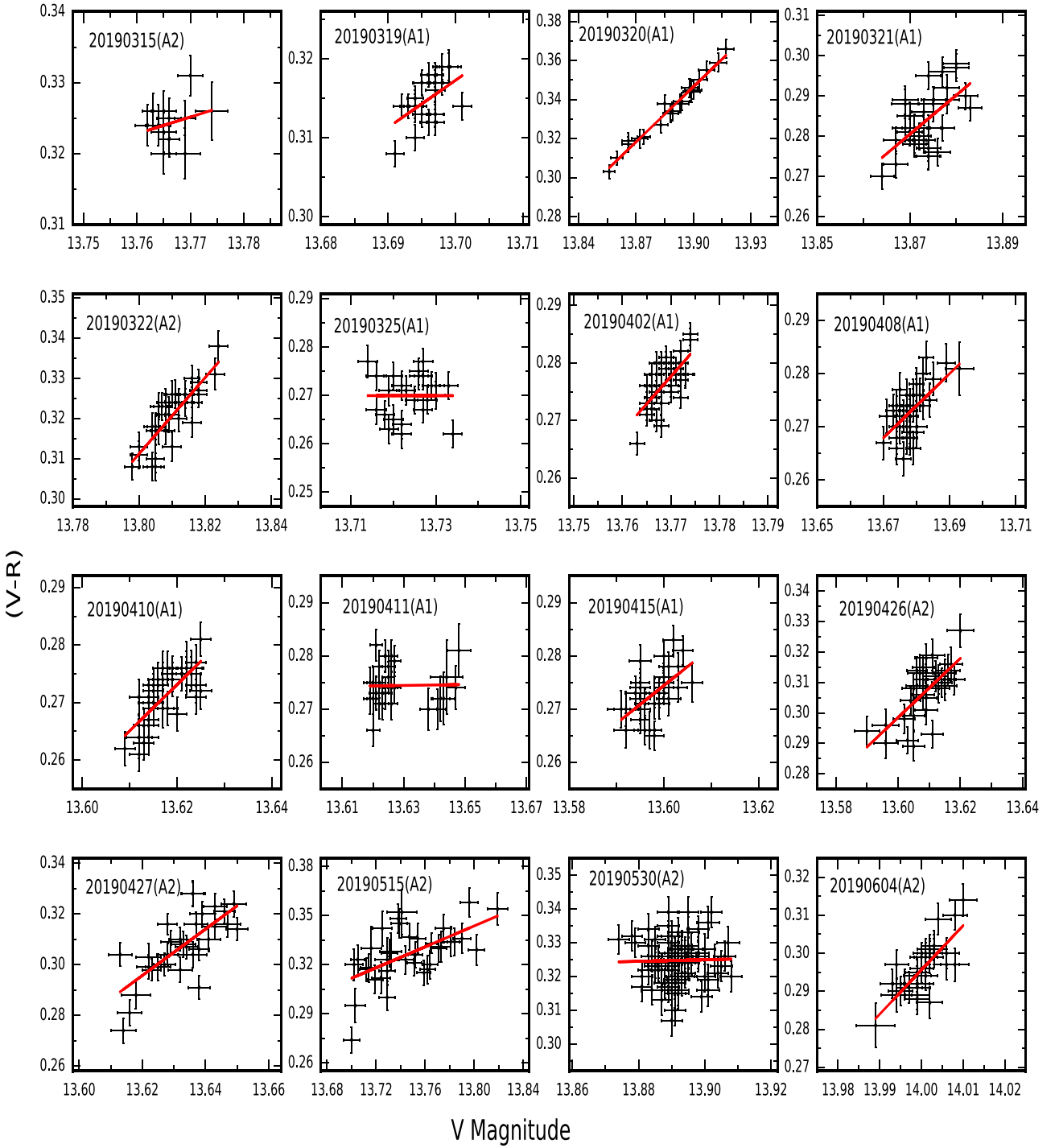
Figure 3. IDV CM plots for PG 1553 + 113. The observation date and the telescope code are given in each plot.

4.3 Spectral energy distribution

To study spectral variations during our observing period, we extracted the optical (BVRI) SEDs of the blazar for 42 nights in which observations were performed quasi-simultaneously in all four B, V, R, I wavebands. For this, we first dereddened the calibrated B, V, R, and I magnitudes by subtracting the Galactic extinction, with A_λ having the following values: $A_B = 0.188$ mag, $A_V = 0.142$ mag, $A_R = 0.113$ mag, and $A_I = 0.078$ mag. The val-

ues of A_λ were taken from the NASA Extragalactic Database (NED).[6] The dereddened calibrated magnitudes in each band were then converted into corresponding extinction corrected flux densities, F_ν. We measured the source's brightest and faintest fluxes on 2019 April 18 and August 14, respectively. The optical SEDs of PG

Table 3. Linear fits to colour–magnitude plots.

Observation date yyyy-mm-dd	m_1 [a]	c_1 [a]	r_1 [a]	p_1 [a]
2019-03-15	0.236	− 2.927	0.267	3.968e-01
2019-03-19	0.596	− 7.847	0.495	1.021e-02
2019-03-20	0.942	− 12.752	0.988	3.677e-16
2019-03-21	0.968	− 13.158	0.596	4.971e-04
2019-03-22	0.948	− 12.796	0.838	3.876e-09
2019-03-25	0.000	0.272	0.000	9.992e-01
2019-04-02	0.955	− 12.874	0.675	4.429e-06
2019-04-08	0.602	− 7.972	0.607	2.533e-05
2019-04-10	0.805	− 10.702	0.742	1.405e-07
2019-04-11	0.008	0.162	0.019	9.151e-01
2019-04-15	0.713	− 9.392	0.576	6.848e-04
2019-04-26	0.973	− 12.895	0.699	8.376e-06
2019-04-27	0.915	− 12.172	0.723	6.291e-06
2019-05-15	0.319	− 4.059	0.585	1.775e-04
2019-05-30	0.023	− 0.002	0.024	8.296e-01
2019-06-04	1.164	− 16.009	0.765	1.301e-07

[a] m_1 = slope and c_1 = intercept of CI against V-mag; r_1 = Correlation coefficient; p_1 = null hypothesis probability.

$1553 + 113$, in $\log(\nu)$ versus $\log(F_\nu)$ representation, are plotted in Fig. 7.

Since a simple power law ($F_\nu \propto \nu^{-\alpha}$), where α is known as the optical spectral index usually provides a good fit to the blazar optical continuum spectra (Hu et al. 2006; Gaur et al. 2012c), we fitted each SED with a first-order polynomial of the form $\log(F_\nu) = -\alpha \log(\nu) + C$ to get the optical spectral indices. The results of the fits are given in Table 6.

The values of the spectral indices (α) range from 0.878 ± 0.029 to 1.106 ± 0.065 and their weighted mean was 0.94 ± 0.033. This value of the spectral index that we got is close to the results found earlier
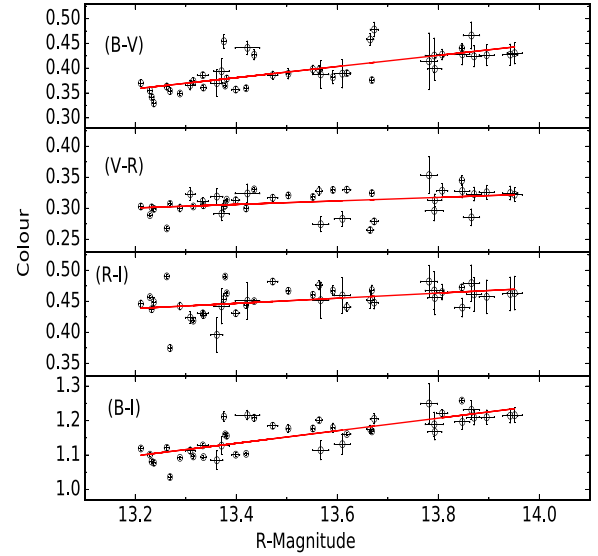
Figure 5. Optical CM plots of PG 1553 + 113 during our total observation duration.

(Falomo, Scarpa & Bersanelli 1994; Agarwal et al. 2021). We show the spectral indices of PG 1553 + 113 with respect to time and R-band magnitude in the top and bottom panels of Fig. 8, respectively. We fitted each panel in Fig. 8 with a first-order polynomial to investigate any variations in the spectral index and fitting results are provided in Table 7. The optical spectral index increases with time and it also shows significant positive correlations with R-band magnitude. The study of MW SEDs can provide important information about physical parameters such as the magnetic field of the emitting region of the source.
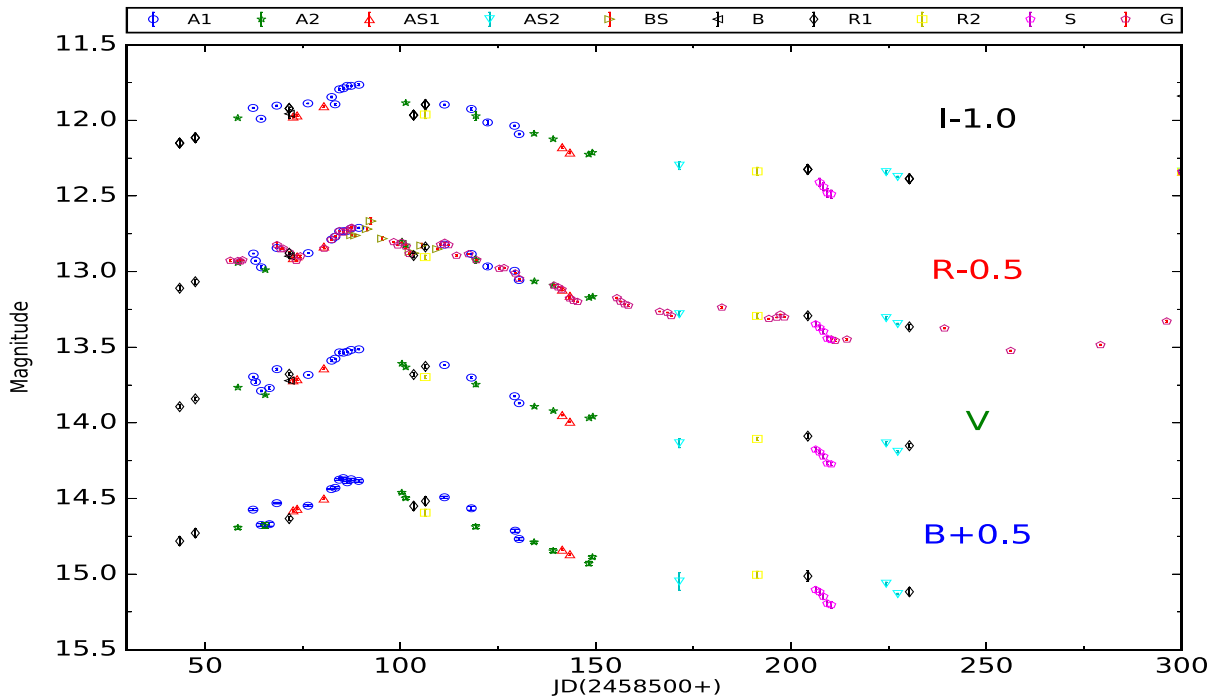
Figure 4. STV optical (BVRI) light curves of PG 1553 + 113, the telescopes, identified by different colours and symbols, are noted at the top of the figure.
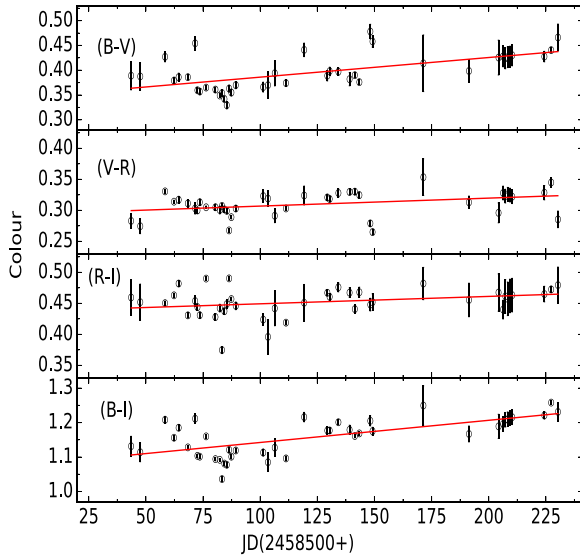
Figure 6. Optical colour variability LCs covering the total observation duration of PG 1553 + 113.

Table 4. Colour–magnitude dependencies and colour–magnitude correlation coefficients on short time-scales.

Colour index	$m_1{}^a$	$c_1{}^a$	$r_1{}^a$	$p_1{}^a$
B−I	0.182	−1.308	0.775	1.7e-07
R−I	0.041	−0.109	0.418	0.006
V−R	0.028	−0.074	0.332	0.032
B−V	0.112	−1.125	0.714	1.1e-07

^{a} m_1 = slope and c_1 = intercept of CI against R-mag; r_1 = Correlation coefficient; p_1 = null hypothesis probability.

Table 5. Colour variation with respect to time on STV time-scales.

Colour index	$m_1{}^a$	$c_1{}^a$	$r_1{}^a$	$p_1{}^a$
B−I	0.0006	1.077	0.678	7.9e-05
R−I	0.0001	0.437	0.297	0.055
V−R	0.0001	0.294	0.374	0.015
B−V	0.0004	0.346	0.622	1.2e-05

^{a} m_1 = slope and c_1 = intercept of CI against Time; r_1 = Correlation coefficient; p_1 = null hypothesis probability.

5 DISCUSSION AND CONCLUSIONS

In this work we analysed the optical photometric data from PG 1553 + 113, a TeV blazar, collected using 10 ground-based telescopes during February–November 2019. In particular, we studied the flux and spectral variability properties of this blazar on both IDV and STV time-scales. We examined a total of 27 optical R-band, 17 in V-band, and 6 in I-band IDV LCs using two statistical methods: the power-enhanced F-test and the nested ANOVA test. We saw robust variability in 4 nights in R-band, and 1 in both V-band and I-band. Only one of these 27 intra-day LCs exhibits statistically significant IDV in all three bands and the amplitude of variability was only 11.82, 9.02, and 8.19 per cent, respectively. So from our IDV analysis, we conclude that optical LCs of PG 1553 + 113 are either constant or show nominal variations on IDV time-scales. As the blazar PG 1553 + 113 did not show large-amplitude variations during our monitoring period, we did not detect significant variations in colour with time (light curve) during our individual nightly observations.
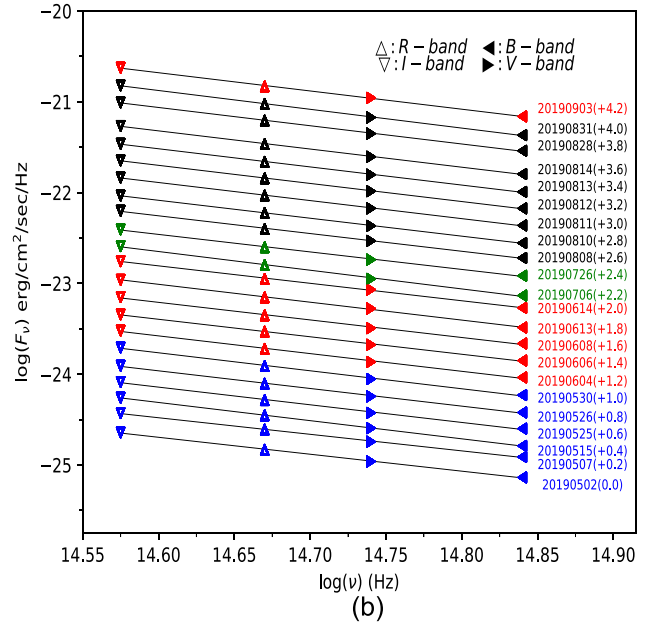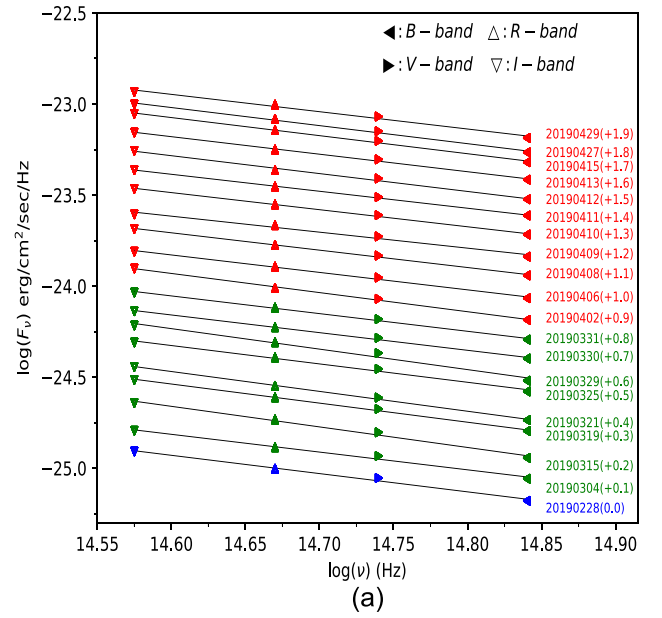

(a)

(b)

Figure 7. The SED of PG 1553 + 113 in B-, V-, R-, and I-bands.

There is one important caveat here: since the durations of our observations are 1.5–5 h, it is certainly possible that if we had longer nightly stares at this source we would have seen more frequent IDV. For example, when the observation period was extended from ≤ 3 to ≥ 6 h, the chances of IDV being found in a group of blazars increased from 64 per cent to 82 per cent (Gupta & Joshi 2005). We used a DCF analysis technique to search for any variability time-scale or periodicity, as well as any possible correlation between different optical energy bands. We found a strong positive correlation, with no significant time lags between the different energy bands, which means that the emission region is the same these wavelengths. The correlation between different energy bands also indicates that the emission is produced by the same electron populations.

Flux variations on an STV time-scale were also seen at all four optical wavelengths (I, R, V, and B), while the colours were found

**Table 6.** Straight-line fits to optical SEDs of TeV blazar PG 1553 + 113.

Observation date yyyy-mm-dd	m_1[a]	c_1[a]	r_1[a]	p_1[a]	Observation date yyyy-mm-dd	m_1[a]	c_1[a]	r_1[a]	p_1[a]
2019-02-28	−1.004	−10.276	−0.995	0.004	2019-05-07	−0.961	−10.591	−0.994	0.005
2019-03-04	−0.975	−10.679	−0.994	0.005	2019-05-15	−1.138	−7.835	−0.993	0.007
2019-03-15	−1.129	−8.371	−0.994	0.005	2019-05-25	−1.081	−8.499	−0.998	0.002
2019-03-19	−1.124	−8.409	−0.991	0.009	2019-05-26	−1.081	−8.327	−0.997	0.003
2019-03-21	−1.048	−9.524	−0.998	0.001	2019-05-30	−1.117	−7.589	−0.998	0.002
2019-03-25	−0.958	−10.837	−0.996	0.003	2019-06-04	−1.087	−7.846	−0.998	0.001
2019-03-29	−1.091	−8.944	−0.998	0.001	2019-06-06	−1.062	−8.022	−0.996	0.003
2019-03-30	−1.009	−10.092	−0.995	0.004	2019-06-08	−1.071	−7.711	−0.998	0.001
2019-03-31	−0.972	−10.692	−0.997	0.002	2019-06-13	−1.106	−6.998	−0.984	0.016
2019-04-02	−1.051	−9.491	−0.998	0.001	2019-06-14	−1.058	−7.493	−0.985	0.015
2019-04-06	−0.953	−10.884	−0.998	0.001	2019-07-06	−1.196	−5.321	−0.998	0.002
2019-04-08	−0.938	−11.084	−0.998	0.001	2019-07-26	−1.064	−7.063	−0.996	0.004
2019-04-09	−0.931	−11.182	−0.999	0.001	2019-08-08	−1.089	−6.494	−0.993	0.006
2019-04-10	−0.992	−10.281	−0.997	0.003	2019-08-10	−1.111	−5.999	−0.993	0.007
2019-04-11	−0.951	−10.957	−0.992	0.007	2019-08-11	−1.126	−5.588	−0.995	0.005
2019-04-12	−0.981	−10.449	−0.995	0.004	2019-08-12	−1.131	−5.341	−0.994	0.005
2019-04-13	−0.992	−10.331	−0.996	0.003	2019-08-13	−1.135	−5.082	−0.995	0.005
2019-04-15	−0.962	−10.732	−0.997	0.002	2019-08-14	−1.137	−4.860	−0.995	0.005
2019-04-27	−0.878	−11.994	−0.991	0.009	2019-08-28	−1.146	−4.462	−0.995	0.004
2019-04-29	−0.971	−10.672	−0.997	0.002	2019-08-31	−1.153	−3.404	−0.995	0.004
2019-05-02	−1.001	−10.213	−0.994	0.005	2019-09-03	−1.145	−4.102	−0.990	0.011

[a] m_1 = slope and c_1 = intercept of $log(F_\nu)$ against $log(\nu)$; r_1 = Correlation coefficient; p_1 = null hypothesis probability.

Table 7. Variation of optical spectral index (α), with respect to R-magnitude and STV time-scale.

Parameters	m	c	r	p
α vs Time	0.0009	0.935	0.673	1.04e-06
α vs R_{mag}	0.2608	−2.492	0.771	2.39e-08

m = slope and c = intercept of α against R-mag and JD; r = Correlation coefficient; p = null hypothesis probability.
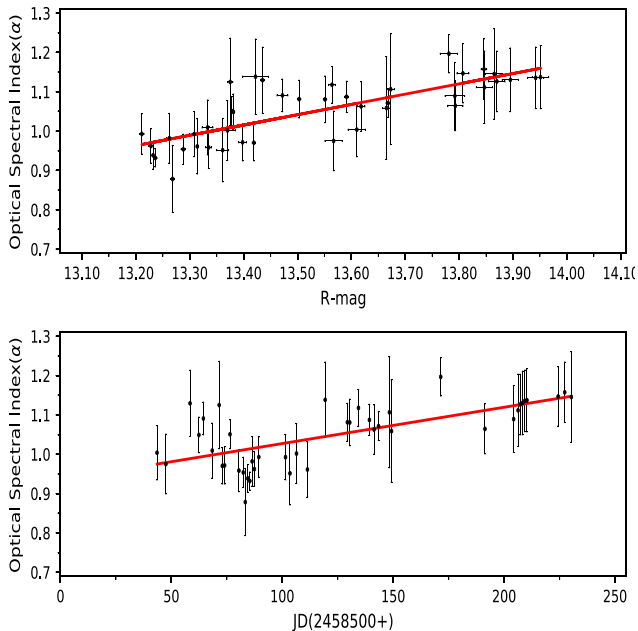
Figure 8. Variation of optical spectral index (α) of PG 1553 + 113 with respect to R-magnitude (top) and time (bottom).

to be non-variable. An earlier optical photometric study of PG 1553 + 113 was carried out by Gaur et al. (2012c). They observed the blazar for IDV on six nights but found no significant IDV or colour (B−R) variability during any night. On STV time-scales they detected genuine flux variability with no variation in colour. Gupta et al. (2016a) also monitored this source for IDV on seven nights but found significant variations on IDV time-scale only on one night. They reported significant flux variability with moderate colour variation on STV time-scales. To find the optical spectral index(α) we made optical SEDs using quasi-simultaneous observation of B, V, R, and I optical band at different times. The optical spectral index (α) showed positive correlations with time and R-band magnitude. The weighted mean value of α is 0.94 ± 0.033 over this STV time-scale.

Studies of flux variability on diverse time-scales is a powerful method to understand the radiation mechanisms of blazars: they can provide information about the size, location, and dynamics of the emitting regions (Ciprini et al. 2003). In blazars, the thermal radiation from the accretion disk is generally overwhelmed by the Doppler-boosted non-thermal radiation from the relativistic jet, so the variability on any measurable time-scale is most likely explained by the relativistic jet based models. On IDV time-scales, blazar variability can reasonably be explained by the shock-in-jet model (e.g. Agarwal & Gupta 2015). However, in the low states of blazars, the variability may be explained by hotspots on, or instabilities in, the accretion discs (e.g. Chakrabarti & Wiita 1993; Mangalam & Wiita 1993). Different models can explain the presence of IDV/STV in the optical (and other) band based on the turbulence behind the shock, or other irregularities in the jet flow produced by variations in the outflow parameters (e.g. Marscher 2014; Calafut & Wiita 2015). Different optical IDV behaviours have been observed in the LBLs and HBLs subclasses of blazars, with HBLs being relatively less variable in optical bands on IDV time-scales than in X-rays and γ-rays (e.g. Heidt & Wagner 1996; Gopal-Krishna et al. 2011; Gupta et al. 2016b). The presence of strong magnetic fields in the relativistic jet could be responsible for the different optical microvariability behaviours of LBLs and HBLs (Romero et al. 1999). Stronger

magnetic fields in HBLs might interrupt the development of small fluctuation by Kelvin Helmholtz instabilities in jets which could interact with the shocks in jets to produce microvariability if the field strength is greater than the critical value B_c given by (Romero 2005).

$$B_c = \left[4\pi n_e m_e c^2(\gamma^2 - 1)\right]^{1/2} \gamma^{-1}, \tag{6}$$

where n_e is the local electron density, m_e is the rest mass of electron, and γ is the bulk Lorentz factor of the flow.

Colour or spectral behaviour are very useful for understanding the emission mechanism of blazars. As mentioned earlier, blazars generally show one of two different colour behaviours, namely bluer-when-brighter (BWB) and RWB. But in some cases, no colour trend behaviour is seen (Böttcher et al. 2009). In BL Lacs, the BWB trend is predominantly found, whereas the FSRQs usually follow the RWB trend (e.g. Gaur et al. 2012a, 2015). Synchrotron models dominated by one component can explain the BWB behaviour if the energy distribution of injected fresh electrons, which cause an increase in flux, is harder (Kirk, Rieger & Mastichiadis 1998). When PG 1553 + 113 exhibited IDV during our observations, it has nearly always follows the BWB trend meaning that the increasing flux can be explained by jet synchrotron emission which indicates that particle acceleration efficiency is enhanced (Agarwal et al. 2015).

From Fig. 8 we see that as the magnitude increases (or this source dims) the spectrum becomes steeper, and this equivalent way of looking at the BWB trend can also be explained by invoking two components: one is a stable component ($\alpha_{constant}$) and the other contributor to the overall optical emission is a variable component with a flatter slope (α_1). Blazars show chromatic behaviours when the variable component dominates over the stable component. On short time-scales, optical variations can be interpreted as arising from strong chromatic components while long-term optical variations can be interpreted in terms of a mildly chromatic component (Villata et al. 2004b). But sometimes, when different pairs of filters are used for colour index measurements, the same source can simultaneously show both BWB and RWB trends (Wu et al. 2011).

ACKNOWLEDGEMENTS

DATA AVAILABILITY

The data in this article will be shared after one year of the publication of the paper at the reasonable request of the corresponding author.

REFERENCES

Ackermann M. et al., 2015, ApJ, 813, L41
Agarwal A., Gupta A. C., 2015, MNRAS, 450, 541
Agarwal A. et al., 2015, MNRAS, 451, 3882
Agarwal A. et al., 2016, MNRAS, 455, 680
Agarwal A. et al., 2019, MNRAS, 488, 4093
Agarwal A. et al., 2021, A&A, 645, A137
Aharonian F. et al., 2006, A&A, 448, L19
Andruchow I., Combi J. A., Muñoz-Arjonilla A. J., Romero G. E., Cellone S. A., Martí J., 2011, A&A, 531, A38
Bachev R., Semkov E., Strigachev A., Gupta A. C., Gaur H., Mihov B., Boeva S., Slavcheva-Mihova L., 2012, MNRAS, 424, 2625
Bachev R. et al., 2017, MNRAS, 471, 2216
Bai J. M., Xie G. Z., Li K. H., Zhang X., Liu W. W., 1998, A&AS, 132, 83
Böttcher M. et al., 2009, ApJ, 694, 174
Calafut V., Wiita P. J., 2015, J. Astrophys. Astron., 36, 255
Carini M. T., Miller H. R., Goodrich B. D., 1990, AJ, 100, 347
Carini M. T., Miller H. R., Noble J. C., Goodrich B. D., 1992, AJ, 104, 15
Chakrabarti S. K., Wiita P. J., 1993, ApJ, 411, 602
Ciprini S., Tosti G., Raiteri C. M., Villata M., Ibrahimov M. A., Nucciarelli G., Lanteri L., 2003, A&A, 400, 487
Clements S. D., Carini M. T., 2001, AJ, 121, 90
Covino S., Landoni M., Sandrinelli A., Treves A., 2020, ApJ, 895, 122
de Diego J. A., 2014, AJ, 148, 93
de Diego J. A., Dultzin-Hacyan D., Ramírez A., Benítez E., 1998, ApJ, 501, 69
de Diego J. A., Polednikova J., Bongiovanni A., Pérez García A. M. , De Leo M. A., Verdugo T., Cepa J., 2015, AJ, 150, 44
Dhiman V., Gupta A. C., Gaur H., Wiita P. J., 2021, MNRAS, 506, 1198
Edelson R. A., Krolik J. H., 1988, ApJ, 333, 646
Falomo R., Treves A., 1990, PASP, 102, 1120
Falomo R., Scarpa R., Bersanelli M., 1994, ApJS, 93, 125
Fan J. H. et al., 1997, A&AS, 125, 525
Fan J. H. et al., 1998, ApJ, 507, 173
Fan J. H., Qian B. C., Tao J., 2001, A&A, 369, 758
Fossati G. et al., 1998, MNRAS, 299, 433
Gaur H., Gupta A. C., Wiita P. J., 2012a, AJ, 143, 23
Gaur H. et al., 2012b, MNRAS, 420, 3147
Gaur H. et al., 2012c, MNRAS, 425, 3002
Gaur H. et al., 2015, MNRAS, 452, 4263
Gaur H. et al., 2019, MNRAS, 484, 5633
Ghosh K. K., Ramsey B. D., Sadun A. C., Soundararajaperumal S., Wang J., 2000, ApJ, 537, 638
Gopal-Krishna, Sagar R., Wiita P. J., 1993, MNRAS, 262, 963
Gopal-Krishna, Goyal A., Joshi S., Karthick C., Sagar R., Wiita P. J., Anupama G. C., Sahu D. K., 2011, MNRAS, 416, 101
Goyal A., Mhaskey M., Gopal-Krishna, Wiita P. J., Stalin C. S., Sagar R., 2013, J. Astrophys. Astron., 34, 273
Green R. F., Schmidt M., Liebert J., 1986, ApJS, 61, 305

Gu M. F., Lee C.-U., Pak S., Yim H. S., Fletcher A. B., 2006, A&A, 450, 39

Gupta A. C., Joshi U. C., 2005, A&A, 440, 855

Gupta A. C., Banerjee D. P. K., Ashok N. M., Joshi U. C., 2004, A&A, 422, 505

Gupta A. C., Fan J. H., Bai J. M., Wagner S. J., 2008, AJ, 135, 1384

Gupta A. C. et al., 2016a, MNRAS, 458, 1127

Gupta A. C., Kalita N., Gaur H., Duorah K., 2016b, MNRAS, 462, 1508

Gupta A. C. et al., 2017, MNRAS, 465, 4423

Gupta A. C. et al., 2019, AJ, 157, 95

Heidt J., Wagner S. J., 1996, A&A, 305, 42

Hu S. M., Zhao G., Guo H. Y., Zhang X., Zheng Y. G., 2006, MNRAS, 371, 1243

Hufnagel B. R., Bregman J. N., 1992, ApJ, 386, 473

Jannuzi B. T., Smith P. S., Elston R., 1994, ApJ, 428, 130

Johnson S. D. et al., 2019, ApJ, 884, L31

Joshi R., Chand H., Gupta A. C., Wiita P. J., 2011, MNRAS, 412, 2717

Kirk J. G., Rieger F. M., Mastichiadis A., 1998, A&A, 333, 452

Kshama S. K., Paliya V. S., Stalin C. S., 2017, MNRAS, 466, 2679

Mangalam A. V., Wiita P. J., 1993, ApJ, 406, 420

Marscher A. P., 2014, ApJ, 780, 87

Massaro E., Nesci R., Maesano M., Montagni F., D'Alessio F., 1998, MNRAS, 299, 47

Miller H. R., Green R. F., 1983, BAAS, 15, 957

Miller H. R., Carini M. T., Goodrich B. D., 1989, Nature, 337, 627

Padovani P., Giommi P., 1995, MNRAS, 277, 1477

Pandey A., Gupta A. C., Wiita P. J., 2017, ApJ, 841, 123

Pandey A., Gupta A. C., Wiita P. J., Tiwari S. N., 2019, ApJ, 871, 192

Pandey A., Gupta A. C., Damljanovic G., Wiita P. J., Vince O., Jovanovic M. D., 2020a, MNRAS, 496, 1430

Pandey A. et al., 2020b, ApJ, 890, 72

Papadakis I. E., Boumis P., Samaritakis V., Papamastorakis J., 2003, A&A, 397, 565

Papadakis I. E., Villata M., Raiteri C. M., 2007, A&A, 470, 857

Pasierb M. et al., 2020, MNRAS, 492, 1295

Peñil P. et al., 2020, ApJ, 896, 134

Polednikova J. et al., 2016, MNRAS, 460, 3950

Prokhorov D. A., Moraghan A., 2017, MNRAS, 471, 3036

Raiteri C. M., Ghisellini G., Villata M., de Francesco G., Lanteri L., Chiaberge M., Peila A., Antico G., 1998, A&AS, 127, 445

Raiteri C. M. et al., 2001, A&A, 377, 396

Raiteri C. M., Villata M., Capetti A., Heidt J., Arnaboldi M., Magazzù A., 2007, A&A, 464, 871

Raiteri C. M. et al., 2015, MNRAS, 454, 353

Rani B. et al., 2010, MNRAS, 404, 1992

Romero G. E., 2005, Chin. J. Astron. Astrophys. Suppl., 5, 110

Romero G. E., Cellone S. A., Combi J. A., 1999, A&AS, 135, 477

Sagar R., Gopal-Krishna, Wiita P. J., 1996, MNRAS, 281, 1267

Sandrinelli A., Covino S., Treves A., Holgado A. M., Sesana A., Lindfors E., Ramazani V. F., 2018, A&A, 615, A118

Sillanpaa A. et al., 1996a, A&A, 305, L17

Sillanpaa A. et al., 1996b, A&A, 315, L13

Stalin C. S., Gopal-Krishna, Sagar R., Wiita P. J., 2004, MNRAS, 350, 175

Stalin C. S., Gupta A. C., Gopal-Krishna, Wiita P. J., Sagar R., 2005, MNRAS, 356, 607

Stetson P. B., 1987, PASP, 99, 191

Stetson P. B., 1992, in Worrall D. M., Biemesderfer C., Barnes J., eds, ASP Conf. Ser. Vol. 25, Astronomical Data Analysis Software and Systems I. Astron. Soc. Pac., San Francisco, p. 297

Tavani M., Cavaliere A., Munar-Adrover P., Argan A., 2018, ApJ, 854, 11

Urry C. M., Padovani P., 1995, PASP, 107, 803

Villata M. et al., 2002, A&A, 390, 407

Villata M. et al., 2004a, A&A, 421, 103

Villata M. et al., 2004b, A&A, 424, 497

Villata M. et al., 2006, A&A, 453, 817

Wagner S. J., Witzel A., 1995, ARA&A, 33, 163

Wu J., Zhou X., Ma J., Jiang Z., 2011, MNRAS, 418, 1640

Xie G. Z., Li K. H., Liu F. K., Lu R. W., Wu J. X., Fan J. H., Zhu Y. Y., Cheng F. Z., 1992, ApJS, 80, 683

Xie G. Z., Li K. H., Zhang Y. H., Liu F. K., Fan J. H., Wang J. C., 1994, A&AS, 106, 361

Xie G. Z., Zhou S. B., Dai B. Z., Liang E. W., Li K. H., Bai J. M., Xing S. Y., Liu W. W., 2002, MNRAS, 329, 689

APPENDIX A: OBSERVATION LOG

Table A1. Observation log for PG 1553 + 113.

Observation date yyyy-mm-dd	Telescope	Data points B, V, R, I	Observation date yyyy-mm-dd	Telescope	Data points B, V, R, I	Observation date yyyy-mm-dd	Telescope	Data points B, V, R, I
2019-02-28	R1	2, 2, 2, 2	2019-04-14	BS	0, 0, 43, 0	2019-06-05	G	0, 0, 5, 0
2019-03-04	R1	2, 2, 2, 2	2019-04-14	G	0, 0, 4, 0	2019-06-06	G	0, 0, 4, 0
2019-03-13	G	0, 0, 5, 0	2019-04-15	A1	1,31, 31, 31	2019-06-06	AS2	1, 1, 1, 1
2019-03-15	A2	1,12,12, 1	2019-04-17	BS	0, 0, 48, 0	2019-06-08	AS2	1, 2, 2, 2
2019-03-15	G	0, 0, 5, 0	2019-04-18	BS	0, 0,103, 0	2019-06-08	G	0, 0, 6, 0
2019-03-16	G	0, 0, 7, 0	2019-04-21	BS	0, 0, 31, 0	2019-06-09	G	0, 0, 4, 0
2019-03-17	G	0, 0, 3, 0	2019-04-24	G	0, 0, 3, 0	2019-06-10	G	0, 0, 4, 0
2019-03-19	A1	1, 26, 26, 1	2019-04-25	G	0, 0, 4, 0	2019-06-13	A2	1, 2,124, 1
2019-03-20	A1	0, 20, 20, 0	2019-04-26	G	0, 0, 4, 0	2019-06-14	A2	1, 2, 82, 1
2019-03-21	A1	1, 30, 30, 1	2019-04-26	A2	1,32, 32, 0	2019-06-20	G	0, 0, 3, 0
2019-03-22	A2	4, 31, 31, 0	2019-04-27	A2	1,30, 30, 30	2019-06-21	G	0, 0, 4, 0
2019-03-24	A1	1, 1, 0, 0	2019-04-27	G	0, 0, 3, 0	2019-06-22	G	0, 0, 4, 0
2019-03-25	A1	1, 24, 24, 1	2019-04-28	G	0, 0, 6, 0	2019-06-23	G	0, 0, 2, 0
2019-03-25	G	0, 0, 8, 0	2019-04-28	BS	0, 0, 35, 0	2019-07-01	G	0, 0, 2, 0
2019-03-26	G	0, 0, 5, 0	2019-04-29	BS	0, 0, 54, 0	2019-07-03	G	0, 0, 1, 0
2019-03-27	G	0, 0,10, 0	2019-04-29	R1	2, 2, 2, 2	2019-07-04	G	0, 0, 4, 0
2019-03-28	B	0,15,15,15	2019-05-01	BS	0, 0, 32, 0	2019-07-06	AS1	2, 2, 2, 2
2019-03-29	G	0, 0, 5, 0	2019-05-02	R1	2, 2, 2, 2	2019-07-17	G	0, 0, 3, 0
2019-03-29	R1	3, 3, 3, 3	2019-05-02	R2	2, 2, 2, 2	2019-07-26	R2	2, 2, 2, 2
2019-03-30	AS2	1, 3, 2, 2	2019-05-05	BS	0, 0, 29, 0	2019-07-29	G	0, 0, 4, 0
2019-03-30	G	0, 0, 5, 0	2019-05-06	G	0, 0, 5, 0	2019-07-31	G	0, 0, 1, 0
2019-03-31	AS2	1, 1, 1, 1	2019-05-07	A1	2, 2, 2, 2	2019-08-01	G	0, 0, 4, 0
2019-03-31	G	0, 0, 5, 0	2019-05-07	G	0, 0, 2, 0	2019-08-02	G	0, 0, 4, 0
2019-04-02	A1	2, 37, 37, 2	2019-05-08	G	0, 0, 4, 0	2019-08-08	R1	2, 2, 2, 2
2019-04-06	AS2	1, 1, 1, 1	2019-05-10	G	0, 0, 4, 0	2019-08-10	S	0, 3, 3, 3
2019-04-07	G	0, 0, 5, 0	2019-05-13	G	0, 0, 4, 0	2019-08-11	S	3, 3, 3, 3
2019-04-08	G	0, 0, 5, 0	2019-05-14	A1	1, 1, 1, 1	2019-08-12	S	3, 3, 3, 3
2019-04-08	A1	1, 41, 41, 41	2019-05-15	A2	1,36, 36, 36	2019-08-13	S	3, 3, 3, 3
2019-04-09	G	0, 0, 6, 0	2019-05-15	G	0, 0, 4, 0	2019-08-14	S	3, 3, 3, 3
2019-04-09	A1	2, 2, 2, 2	2019-05-18	A1	0, 0, 1, 1	2019-08-14	G	0, 0, 2, 0
2019-04-10	G	0, 0, 8, 0	2019-05-21	G	0, 0, 4, 0	2019-08-15	G	0, 0, 3, 0
2019-04-10	A1	1, 37, 37, 37	2019-05-23	G	0, 0, 3, 0	2019-08-18	G	0, 0, 3, 0
2019-04-11	G	0, 0, 4, 0	2019-05-25	G	0, 0, 4, 0	2019-08-28	AS1	2, 2, 2, 2
2019-04-11	A1	2, 32, 32, 30	2019-05-25	A1	2, 1, 1, 1	2019-08-31	AS1	2, 2, 2, 2
2019-04-12	A1	2, 2, 2, 2	2019-05-26	A1	1, 2, 2, 1	2019-09-03	R1	2, 2, 2, 2
2019-04-12	G	0, 0, 8, 0	2019-05-26	G	0, 0, 4, 0	2019-09-12	G	0, 0, 3, 0
2019-04-13	G	0, 0, 4, 0	2019-05-30	A2	1,82, 82, 1	2019-09-29	G	0, 0, 3, 0
2019-04-13	A1	2, 2, 2, 2	2019-06-04	A2	1,34, 34, 1	2019-10-22	G	0, 0, 5, 0
2019-04-13	BS	0, 0, 29, 0	2019-06-04	G	0, 0, 5, 0	2019-11-08	G	0, 0, 5, 0

APPENDIX B: RESULTS OF IDV

Table B1. Results of IDV analysis of PG 1553 + 113.

Observation date yyyy-mm-dd	Band	Power-enhanced F-test			Nested ANOVA			Status	Amplitude
		DoF(v_1, v_2)	F_{enh}	F_c	DoF(v_1, v_2)	F	F_c		%
20190315	V	11, 22	1.42	3.18	2, 9	1.98	8.02	NV	–
	R	11, 22	1.70	3.18	2, 9	2.33	8.02	NV	–
	V−R	11, 22	1.47	3.18	2, 9	0.91	8.02	NV	–
20190319	V	25, 50	0.64	2.16	4, 20	0.87	4.43	NV	–
	R	25, 50	0.84	2.16	4, 20	2.83	4.43	NV	–
	V−R	25, 50	0.64	2.16	4, 20	0.94	4.43	NV	–
20190320	V	19, 38	1.32	2.42	3, 16	0.31	5.29	NV	–
	R	19, 38	1.42	2.42	3, 16	1.76	5.29	NV	–
	V−R	19, 38	0.72	2.42	3, 16	0.81	5.29	NV	–
20190321	V	29, 58	1.89	2.05	5, 24	1.43	3.89	NV	–
	R	29, 58	4.08	2.05	5, 24	2.38	3.89	NV	–
	V−R	29, 58	1.66	2.05	5, 24	1.02	3.89	NV	–
20190322	V	30, 60	1.82	2.03	5, 24	0.52	3.89	NV	–
	R	30, 60	0.48	2.03	5, 24	0.23	3.89	NV	–
	V−R	30, 60	1.15	2.03	5, 24	0.38	3.89	NV	–
20190325	V	23, 46	1.62	2.24	5, 18	2.56	4.25	NV	–
	R	23, 46	1.34	2.24	5, 18	1.33	4.25	NV	–
	V−R	23, 46	1.87	2.24	5, 18	2.32	4.25	NV	–
20190402	V	36, 72	0.74	1.91	6, 28	0.86	3.52	NV	–
	R	36, 72	1.52	1.91	6, 28	7.83	3.52	NV	–
	V−R	36, 72	1.07	1.91	6, 28	5.65	3.52	NV	–
20190408	V	40, 80	2.55	1.85	7, 32	2.57	3.25	NV	–
	R	40, 80	2.18	1.85	7, 32	0.67	3.25	NV	–
	I	40, 80	1.15	1.85	7, 32	1.35	3.25	NV	–
	V−R	40, 80	1.28	1.85	7, 32	2.22	3.25	NV	–
20190410	V	37, 74	0.99	1.89	6, 28	0.62	3.52	NV	–
	R	37, 74	1.22	1.89	6, 28	0.62	3.52	NV	–
	I	37, 74	0.84	1.89	6, 28	1.01	3.52	NV	–
	V−R	37, 74	0.69	1.89	6, 28	0.93	3.52	NV	–
20190411	V	31, 62	0.33	2.01	5, 24	1.58	3.89	NV	–
	R	31, 62	0.42	2.01	5, 24	1.53	3.89	NV	–
	I	29, 58	0.49	2.03	5, 24	1.15	3.89	NV	–
	V−R	31, 62	0.26	2.01	5, 24	2.39	3.89	NV	–
20190413	R	30, 60	0.97	2.03	5, 24	2.65	3.89	NV	–
20190414	R	42, 84	3.66	1.82	7, 32	1.13	3.26	NV	–
20190415	V	30, 60	1.32	2.028	5, 24	5.77	3.89	NV	–
	R	30, 60	1.62	2.028	5, 24	9.87	3.89	NV	–
	I	30, 60	1.54	2.028	5, 24	1.46	3.89	NV	–
	V−R	30, 60	1.48	2.028	5, 24	2.31	3.89	NV	–
20190417	R	47, 94	2.78	1.76	11, 36	9.44	2.79	V	14.98
20190418	R	102,204	2.93	1.48	19,80	4.19	2.14	V	8.89
20190421	R	30, 60	3.81	2.03	5, 24	2.37	3.89	NV	–
20190426	V	31, 62	0.99	2.01	5,24	0.43	3.89	NV	–
	R	31, 62	1.02	2.01	5,24	0.46	3.89	NV	–
	V−R	31, 62	1.23	2.01	5,24	0.35	3.89	NV	–
20190427	V	29, 58	0.86	2.05	5, 24	3.20	3.89	NV	–
	R	29, 58	1.04	2.05	5, 24	1.70	3.89	NV	–
	I	29, 58	0.71	2.05	5, 24	2.30	3.89	NV	–
	V−R	29, 58	1.37	2.05	5, 24	3.49	3.89	NV	–
20190428	R	34, 68	1.25	1.95	6,28	3.58	3.52	NV	–
20190429	R	53, 106	0.56	1.71	9,40	3.91	2.89	NV	–
20190501	R	31, 62	0.59	2.01	5,24	1.99	3.89	NV	–
20190505	R	28, 56	0.92	2.08	4, 20	2.31	4.43	NV	–
20190515	V	35, 70	6.53	1.93	6, 28	10.36	3.52	V	11.82
	R	35, 70	3.13	1.93	6, 28	8.57	3.52	V	9.02
	I	35, 70	3.21	1.93	6, 28	3.75	3.52	V	8.19
	V−R	35, 70	0.82	1.93	6, 28	1.44	3.52	NV	–
20190530	V	81,162	1.29	1.55	15,64	1.25	2.33	NV	–
	R	81,162	1.26	1.55	15,64	1.89	2.33	NV	–
	V−R	81, 162	0.82	1.55	15,64	1.36	2.33	NV	–

Table B1 – *continued*

Observation date	Band	Power-enhanced F-test			Nested ANOVA			Status	Amplitude
yyyy-mm-dd		DoF(ν_1, ν_2)	F_{enh}	F_c	DoF(ν_1, ν_2)	F	F_c		%
20190604	V	33, 66	1.88	1.96	5, 24	1.01	3.89	NV	–
	R	33, 66	0.75	1.96	5, 24	0.94	3.89	NV	–
	V−R	33, 66	0.91	1.96	5, 24	1.04	3.89	NV	–
20190613	R	123, 246	1.97	1.43	23,96	2.65	2.00	V	3.91
20190614	R	81, 162	0.47	1.55	15,64	1.57	2.33	NV	–

This paper has been typeset from a TEX/LATEX file prepared by the author.